https://doi.org/10.1016/j.jpowsour.2022.232592

Regulating the interfacial chemistry enables fast-kinetics hard carbon anodes for potassium ion batteries

*Zhenlu Yu, Qun Liu, Changsheng Chen, Ye Zhu and Biao Zhang**

Department of Applied Physics, The Hong Kong Polytechnic University, Hung Hom, Hong Kong, China.

Abstract

Whether carbon anodes could sustain the high-rate potassium ion batteries (PIBs) remains controversial, owing partly to the distinct electrode preparation protocols and electrolyte systems in reported works. Herein, we adopt a freestanding carbon nanofiber (CNF) film as a model system to explore the charge transfer kinetics in carbon anodes. Without the interference of binders and additives, we probe the effect of interfacial chemistry and boost the kinetics through a tetrahydrofuran-based electrolyte. The weak solvent-cation interaction promotes the rapid desolvation of potassium ions. More importantly, such an electrolyte also benefits the formation of a thin and uniform solid electrolyte interphase. Consequently, the CNFs anode exhibits fast kinetics evidenced by a capacity of 143 mAh g^{-1} at a large current density of 1.5 A g^{-1} (~5.4C) and 200 mAh g^{-1} at a low temperature of 0 °C, significantly outperforming the performance in classical carbonate electrolytes. This work demonstrates the critical roles of electrode/electrode interfaces in determining the stability and kinetics of PIBs.

Keywords: Potassium-ion batteries, Ether-based electrolyte, Solid–electrolyte interphase, Kinetics, Weak solvation

1. Introduction

Cost-effective battery systems are essential to stationary energy storage for promoting clean energy utilization[1]. Novel batteries relying on diverse cations, such as Na^+[2], K^+ [3], Zn^{2+} [4], and Al^{3+} [5], have been investigated due to their unique characteristics of natural abundance, safety, and cost. Among these, potassium-ion batteries (PIBs) are promising supplementary to lithium-ion batteries (LIBs) benefiting from the rich K elements in the earth's crust and the closest standard redox potential of K^+/K (-2.93 V) to Li^+/Li (-3.04 V, both vs. standard hydrogen electrode) [3]. Nevertheless, the large ionic radius of K ion [6] poses challenges to the electrode design and the charge transfer kinetics during insertion/extraction. For instance, the K ions intercalation into graphite anodes could bring a volume expansion of 60% when a stage-I graphite intercalation compound of KC_8 is formed, which is almost six times that for LiC_6 formation in LIBs [7]. Such a large volume change affects both the stability of electrode materials [8] and the solid electrolyte interphases (SEIs) that are covered on the electrode surface. E. Peled proposed the SEI concept in 1979 [9], which consists of electrolyte decomposition products. The critical roles of SEIs in battery stability, rate capability, and safety have been universally recognized throughout the past 40 years of research [10-12]. Besides the radius difference, the un-optimized SEIs are also partly responsible for the poorer rate capability of graphite in PIBs than in LIBs [7].

The large carbon family provides a great opportunity to search for anode candidates other than graphite for improving stability and kinetics [13, 14]. Thanks to extensive efforts in the past several years, a variety of carbon anodes have been developed, with hard carbon being the most widely explored [15-17]. Because of the abundant active sites, the K ions storage in hard carbon normally makes use of several mechanisms instead of intercalation alone [18], thus reducing the volume expansion to increase the structural stability. Despite the enhanced cyclic life, the rate capability of hard carbon anodes remains unsatisfactory. In particular, a large discrepancy in the K ion transfer kinetics has been found [19]. The distinct electrode preparation protocol, including the binder type and amount of conductive additives, is partly responsible for the observations. Except for it, the electrode/electrolyte interfaces also play critical roles, as demonstrated by the huge differences under the several carbonate-based electrolytes [20].

Optimizing electrolyte formulations has been widely adopted to tailor interfacial chemistry. High-concentration electrolytes (HCEs) [21, 22] are utilized to refine the solvation structure, where K^+ is preferentially coordinated with anions instead of the solvent to form contact ion pairs (CIPs) and aggregated ion pairs (AGGs) [23]. Such an alternation has a great impact on the microstructure of SEI through dominant anion decomposition [24]. Considering the high cost of HCE, the ether-based electrolyte is another popular approach to regulate the interfaces at a normal concentration. Linear ether, such as 1,2-dimethoxyethane (DME), has been extensively studied [21, 25]. It helps the stabilization of graphite anode by building robust SEIs. Nevertheless, the extension of DME to hard carbon anode is not very successful until now. One possible reason is the solvent co-intercalation [26], which decreases the capacity of hard carbon and may bring structural deterioration.

In this work, we shift from the linear ether to a cyclic counterpart, i.e., tetrahydrofuran (THF), to prevent solvent co-intercalation and boost the kinetics of hard carbon through interfacial chemistry regulation. To exclude the interference of the binder, we prepare a carbon nanofiber (CNF) film by electrospinning to serve as freestanding electrodes. Thanks to the rapid desolvation process and the stable SEI formation in THF-based electrolytes, the CNFs possess fast kinetics allowing the cycling at high current rates and low temperatures.

2. Experimental section

2.1 Materials synthesis

To prepare the CNFs, 1 g of lignin (kraft, Alfa Aesar) and 0.5 g polyacrylonitrile (PAN, Mw 150,000, Sigma Aldrich) were dissolved and stirred in 10 mL N-dimethylformamide at 60 °C overnight. Afterward, the lignin-PAN solution was electrospun into the nanofiber film under the high voltage of 18 kV with the feed rate of 1 mL h^{-1}, which was collected on the Al foil and peeled off after the electrospinning. Then a stabilization process with a ramping rate of 0.5 °C min^{-1} at 250 °C for 1 h in the muffle oven was applied to improve the thermal stability of PAN during subsequent carbonization. Finally, the CNFs with a yield of 42% were collected after annealing at 1350 °C for 2 h with the heating rate of 3 °C min^{-1} in the tube furnace under Ar flow.

For the preparation of lignin powder-based (LigP) electrode, lignin powder was first pre-treated at 200 °C in air for 1 h and then carbonization at 1350 °C for 2 h under argon. The LigP was then mixed with Super P, carboxymethylcellulose sodium binder in the weight ratio of 8:1:1 in the 1-Methyl-2-pyrrolidone solvent to obtain the slurry.

Afterward, the slurry was cast onto Cu foil followed by drying at 80 °C and cut into Φ12mm discs.

2.2 Electrochemical measurements

CR2032 cells, consisting of CNFs as the freestanding electrode or LigP electrode, one piece of glass fiber (GF/D) as the separator, and K metal foil as both the counter and the reference electrode, were assembled in a glove box (with O_2 and H_2O content below 0.1 ppm). The mass loading of both CNFs and LigP was around 1.0 mg cm^{-2}. 80 μl 1M Potassium bis(fluorosulfonyl)amide (KFSI) in Ethylene carbonate (EC)/dimethyl carbonate (DMC) (1:1 vol%), THF, and DME were selected as the electrolytes. The electrochemical tests at 25 °C and 0 °C were performed on Neware tester in the voltage range of 0-3 V. Galvanostatic Intermittent Titration Technique (GITT) tests were conducted to compare the kinetics between different electrolytes. A current density of 25 mA g^{-1} with a pulse time of 20 min at 2 h intervals was set on both cells after one cycle at 50 mA g^{-1}. Electrochemical Impedance Spectroscopy (EIS) was collected through an electrochemical workstation (CHI760E) in the frequency range from 10^5 to 10^{-2} Hz with a potential amplitude of 5 mV.

2.3 Characterization

The solvation structure of different electrolytes was analyzed through Raman spectroscopy (Witec Confocal Raman, with a 532 nm laser), which was also applied to determine the graphitized degree and monitor the structural evolution of CNFs upon cycling. The morphology and diameter of CNFs were determined through Scanning electron microscopy (SEM) and high-resolution transmission electron microscopy

(HRTEM) at JEOL JEM-2100F. X-ray diffraction (XRD) using Cu Kα radiation (Rigaku SmartLab 9kW) was utilized to obtain the crystalline information. The porosity was examined via N_2 adsorption/desorption through ASAP2020 apparatus. X-ray photoelectron spectroscopy (XPS) was performed by the Thermo Kalpha apparatus to examine the surface element content of CNF electrodes. The electrodes were disassembled from the cells after 3 cycles at 50 mA g^{-1} and washed 5 times with the corresponding solvent in the electrolyte, and then delivered to the XPS chamber using a vacuum transfer unit.

3. Results and discussion

We first compare the physical-chemical properties, including the dielectric constant (ε), donor number (DN), and viscosity of different solvents (Table S1) to search for potential electrolyte formulations in regulating the interfacial chemistry. These parameters could reflect the solvating capability of the solvents to some extent, thus greatly affecting the desolvation and the charge transfer kinetics across the SEIs [27, 28]. The polar solvent EC, a main member of the carbonate family, exhibits an extremely high ε of 89.8 strongly coordinating with K^+. And linear carbonate like DMC usually serves as a supplement for carbonate electrolytes to lower the viscosity of EC. A common electrolyte containing 1M KFSI in EC/DMC (1:1 vol%) is used in this work as the control electrolyte. Ethers usually exhibit lower solvating/desolvating energy than esters and support excellent cycling performance. We first focus on the most popular DME solvent, which has a linear structure, and then compare it with the less explored cyclic THF ether. The two ethers possess similar ε, but the THF has a much lower DN than DME (8 *vs.* 20). In addition, previous studies reveal that the oxygen atom is the most preferred site to coordinate with the cation (K^+) during solvation [29]. Based on the structural skeleton in Table S1, THF only offers one O atom, compared to two in DME, for serving as the potential coordination sites [30]. The above theoretical analysis indicates the THF may exhibit weak cation-solvent intercalation in the electrolytes.

The solvation structure of electrolytes directly affects the interfacial chemistry and electrochemical performance. Raman spectra (Fig. 1a,b) are adopted to investigate the solvation structure in different electrolytes, including 1M KFSI in THF, 1M KFSI in DME, and KFSI in EC/DMC. Specifically, the Raman peak at 700-780 cm^{-1} for KFSI containing different electrolytes results from FSI^- anions. For EC/DMC system, after the addition of KFSI salt, the vibration band of free solvent at 899 cm^{-1} undergoes a right shift, indicating the strong interaction of EC/DMC with K^+. The band centered at 722.1 cm^{-1} becomes wider, signifying the abundant free FSI^- (723 cm^{-1}) without the appearance of CIP (732.8 cm^{-1}) and AGG (742.5 cm^{-1}). It further proves the strong solvation power of EC/DMC, as suggested in previous studies [31]. Additionally, relatively strong solvation of solvent with K^+ can also be found in the DME system: a new vibration band arises at 860 cm^{-1}, which corresponds to the coordinated K^+–DME [27]. However, the FSI^- signal is more complex than that of the EC/DMC system, which will be discussed later. In contrast, for the THF system, the vibration bands at 916 cm^{-1} of pure THF and KFSI-contained THF-based electrolytes are almost coincident, which suggests the weak interaction between K^+ and THF solvent.

To further clarify the complex FSI^{-} signals in the DME system and THF system, the enlarged peaks of S−N−S signal in FSI^{-} anion have been fitted (Fig. 1b). In the DME solvation structure, free FSI^{-} accounts for 47.7% with the low content of CIP (21.2%) and AGG (31.1%) contribution. On the contrary, the solvation structure in the THF electrolyte is dominated by CIP (52.8%) and AGG (33.8%), with only 13.4% of free FSI^{-}. As depicted in the right part of Fig. 1c, the CIP and AGG dominant solvation structure in the THF system implies the stronger coordination power of K^{+-} and anion FSI^{-}, and the lower solvation power of THF solvent. The lower solvation/desolvation power of THF is likely to induce the anion-derived SEI and boost the kinetics [32].

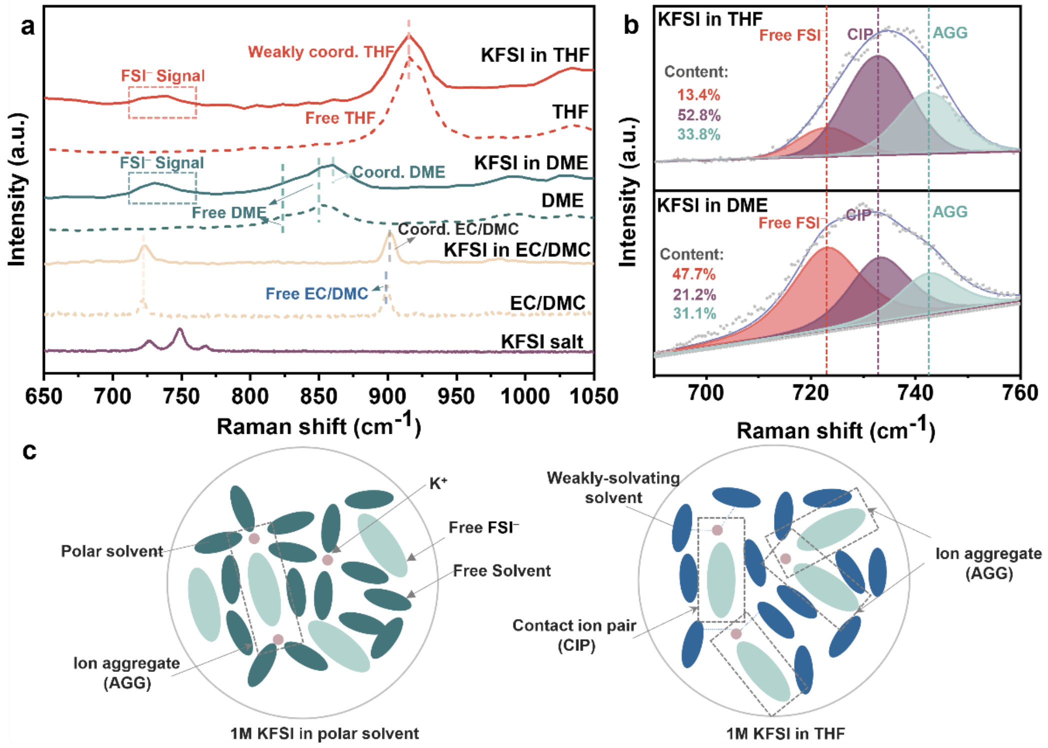

Fig. 1. (a) Raman spectra of electrolytes, pure solvents, and KFSI salt; (b) Enlarged FSI^{-} peaks of 1M KFSI in THF and1M KFSI in DME; (c) Schematic illustration of the solvating structure of 1M KFSI in DME and 1M KFSI in THF.

To reveal the influence of solvation structure on interfacial chemistry and electrochemical performance of anodes, the freestanding CNF electrodes are adopted as the model system (Fig. 2a). A naturally abundant lignin polymer was used as the precursor to produce CNFs. Because of the poor spinnability of pure lignin, a blended lignin/PAN was electrospun and thermal annealed to produce CNF film, as illustrated in Fig. 2a. A high carbon content of 96.8% is observed in the CNFs, as indicated by the XPS in Fig. S1a. The high purity carbon largely precludes the K ion storage through functional groups, which usually takes place at a high potential of over 1 V (*vs.* K/K^+). The CNFs show a surface area of 122.1 m^2 g^{-1} and a pore volume of 0.03 m^3 g^{-1} (Fig. S1). The morphology of CNF is captured through SEM (Fig. 2b) and TEM (Fig. 2c), showing a bead-free structure with a diameter ranging from 221 to 566 nm. There is an absence of clear graphitic structure in the CNFs due to the low carbonization temperature. This is confirmed by the XRD result (Fig. 2d), which exhibits a board (002) peak indicating poor crystallinity with a large d-spacing of 3.85 Å (*vs.* 3.38 Å for graphite). The prominent D-band in the Raman spectrum (Fig. S2b) also suggests that a temperature of 1350 ºC is insufficient to promote graphitization. Nevertheless, a sharp (101) diffraction peak is observed, indicating the presence of tiny graphitic domains.

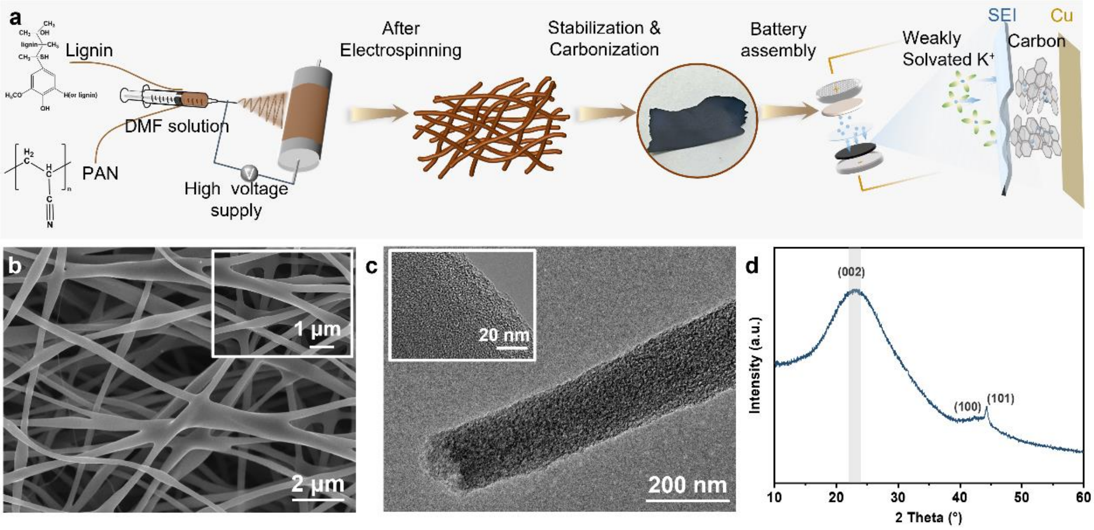

Fig. 2. (a) Fabrication scheme of CNFs for potassium ion batteries; (b) SEM and (c) HRTEM images of CNFs; (d) XRD pattern of CNF.

The electrochemical performance of CNFs in different electrolytes is compared. Surprisingly, it delivers a super-low reversible capacity of 67 mAh g^{-1} in 1M KFSI in DME electrolyte (Fig. S3a). A detailed examination of the voltage profiles by dQ (capacity)/dV(voltage) curve suggests the presence of solvent co-intercalation during K ion insertion, as evidenced by the characteristic peak at ~ 1.16 V [29]. It suggests that the co-intercalation could occur in not only the perfectly ordered graphite anode but also in the hard carbon with tiny graphitic domains. Although it likely does not affect the stability of graphite, the solvent co-intercalation significantly decreases the cyclic life of the CNFs anode. Thanks to the weak K-solvent interaction in the THF electrolyte, there is not any trace of co-intercalation from the voltage profiles (Fig. S3b). It shows a high capacity of 245 mAh g^{-1} in 1M KFSI in THF at 50 mA g^{-1}, which also outperforms the 158 mAh g^{-1} in 1M KFSI in EC/DMC (Fig. 3a). Note that despite the even stronger solvation in EC/DMC than in DME, the solvent co-intercalation rarely takes place in carbonate electrolytes except propylene carbonate [33]. Therefore, we focus on the EC/DMC and THF electrolytes in the following part to probe the effect of interfacial chemistry.

The CNFs deliver an attractive rate performance in 1M KFSI in THF, with a capacity of 245, 205, 186, 175, 157, and 143 mAh g^{-1} at 50, 100, 250, 500, 1000, and 1500 mA g^{-1}, respectively (Fig. 3b). Here 1500 mA g^{-1} corresponds to ~5.4 C based on the theoretical capacity of KC_8 formation (279 mAh g^{-1}). The capacity could fully recover after the current density returns to 50 mA g^{-1}. This performance is superior to most previously reported works (Table S2), especially those with essential K ion insertion with a practicable average potential of < 1 V *vs.* K^+/K. In contrast, the CNFs undergo a fast capacity decrease with the increase in the current density in the electrolyte of 1M KFSI in EC/DMC. A merely 63 mAh g^{-1} of capacity remains at 1000 mA g^{-1}, which further reduces to 31 mAh g^{-1} at 1500 mAh g^{-1}. We note that the different carbonate solvents could also affect the rate capability. A 1M KFSI in EC/ Ethyl methylcarbonate (EMC) electrolyte is assessed (Fig. S4), considering the beneficial effect of EMC in graphite anode [34]. Although a high initial capacity of 266 mAh g^{-1} is achieved in 1M KFSI in EC/EMC at 50 mA g^{-1} for CNF, it sharply declines by over 50% (< 130 mAh g^{-1}) at the current density of 250 mA g^{-1}, which is even poorer than that in 1M KFSI in EC/DMC. Additionally, to examine whether the similar phenomenon occurs in classical electrodes, pure lignin powder-based electrode with a much smaller surface area (12.3 m^2 g^{-1} *vs.* 122.1 m^2 g^{-1} for CNFs) is measured as well (Fig. S5). LigP delivers an initial capacity of 215 mAh g^{-1} at 50 mA g^{-1} in THF electrolyte and maintains over half (119 mAh g^{-1}) when the current density comes to

250 mA g^{-1}. However, the capacity of LigP sharply decreases from 131 mAh g^{-1} at 50 mA g^{-1} to below 50 mAh g^{-1} at 250 mA g^{-1} in EC/DMC system. It confirms the advantage of THF electrolytes in achieving high-rate carbon anodes although the capacity is unsatisfactory in comparison with CNFs. Such an enhancement in the rate capability does not sacrifice stability. The CNF exhibits a stable specific capacity of 232 mAh g^{-1} with a retention of 97% after 50 cycles at 100 mA g^{-1} (Fig. S6).

Pushing to the limit, we examine the performance at a low temperature of 0 °C (Fig. 3c). The electrode delivers a competitive capacity of 200 mAh g^{-1} at 50 mA g^{-1} in 1M KFSI in THF systems, showing superiority in both capacity and stability compared to the one in carbonate electrolytes. GITT tests are applied for CNF electrodes in the two electrolytes to compare the charge transfer kinetics. The diffusivity evolutions with respect to the charging/discharging potential are presented in Fig 3d-e. Upon discharging, the K^+ diffusion coefficient declines gradually in the EC/DMC electrolyte. Compared with the EC/DMC system, the higher coefficient in the THF electrolyte between 1.0-0.5 V (during the SEI formation period) indicates a smoother SEI formation in the THF electrolyte. Nevertheless, there is almost no difference between coefficients in the low-voltage region, likely suggesting that the insertion mechanism is not affected by the disparity in the two electrolytes. The coefficient of K^+ in THF electrolyte is generally half order of magnitude larger than that in carbonate in the following charging process. Additionally, although the original impedance of CNF is over 2000 ohm for both electrolytes (Fig. S7), a drastic decrease of 50% in the impedance of the CNF electrode is found in 1M KFSI in THF after 3 cycles at 100 mA

g^{-1}. In contrast, the impedance R_{ct} remains great (1985 ohm) for CNF in EC/DMC system after 3 cycles. Therefore, a significant boost in kinetic is achieved by changing the EC/DMC electrolyte into the THF electrolyte, which is aligned with the above theoretical analysis.

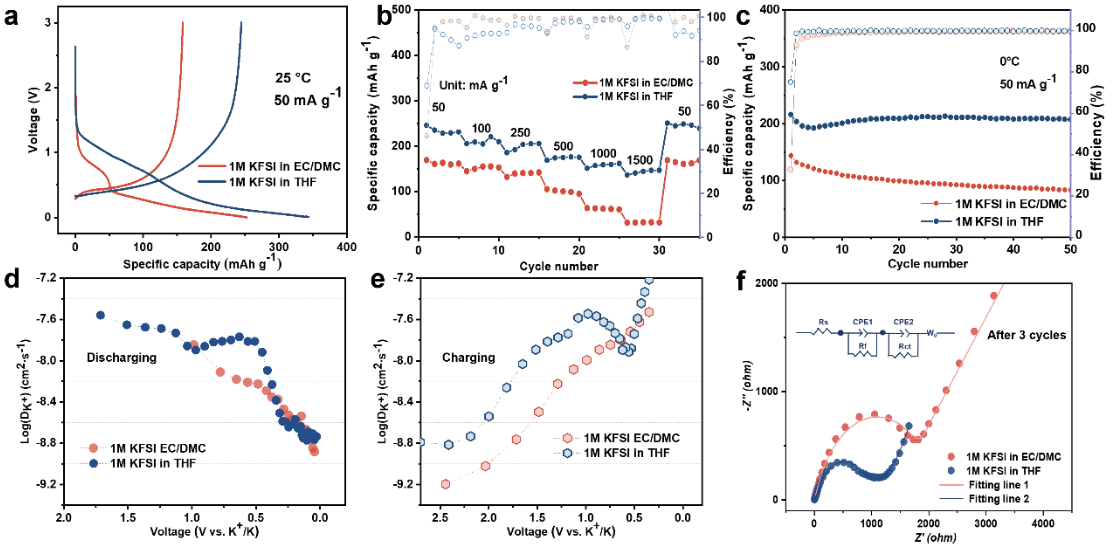

Fig. 3. Electrochemical performances and kinetics of CNF in different electrolytes. (a) Initial charge/discharge profiles at 25 °C; (b) Rate behaviors; (c) Cyclic performances at 0 °C; K ion apparent diffusion coefficient calculated from GITT results of CNF in 1M KFSI in EC/DMC and 1M KFSI in THF upon (d) discharging and (e) charging; (f) EIS plots of CNF electrode after three cycles in different electrolytes at 100 mA g^{-1}.

The reaction kinetics could be affected by both the charge storage mechanism and interface properties. The in-situ Raman is first conducted to distinguish whether the different electrolytes change the K ion insertion behavior. Once discharged in the THF electrolyte (Fig. 4a), the G band at 1598 cm^{-1} of CNF begins to redshift and becomes wider arising from the new splitting peak G_c corresponding to the graphite intercalation compounds (GICs). That results from the intercalation of K^+ and electron conveyed to graphic layers [35-37]. And the gradual blue shift of the G band implies the leaving of K^+ from the graphitic layer during the charging process, which is the typical change for graphitic anodes [38]. These results confirm the neat K ion insertion in THF-electrolyte, in contrast to the solvent co-intercalation in the DME. In EC/DMC system (Fig. S8), the almost identical evolution of the G band for the CNF electrode is found, with the tendency of gradual red shift of the G-band upon discharging and continuous blue shift upon charging. A similar pace of K ion insertion exists in the two electrolyte systems. Therefore, the better kinetics in THF electrolyte arises mainly from the fast interfacial process, involving the de-solvation of K^+ first and then the diffusion across the SEI. As the former Raman analysis of electrolytes demonstrated, the weak K-THF interaction benefits the de-solvation process. We further examine the SEIs formed on CNFs in different electrolytes by HRTEM (Fig. 4b-c). For CNFs cycled in 1M KFSI in THF, a thin and uniform SEI with a thickness of 4.5 nm is covered on the nanofiber. Turning to the SEI formed in 1M KFSI in EC/DMC, it exhibits uneven thickness ranging from 2 to 8.3 nm. In particular, tiny inorganic crystals like K_2SO_4 and K_2O, as identified from the Fast Fourier Transformation (FFT) patterns, are embedded in the SEIs formed in EC/DMC electrolytes. In comparison, there is the absence of crystal phases in the SEIs under THF electrolytes, possibly due to the thin SEIs that restrict the crystallization and growth of inorganic species [39]. The thick and uneven SEI in the carbonate electrolyte would increase the impedance and deteriorate the K^+ transport kinetics [40, 41], explaining the inferior K^+ diffusivity in EC/DMC-based electrolyte despite the same K^+ insertion process.

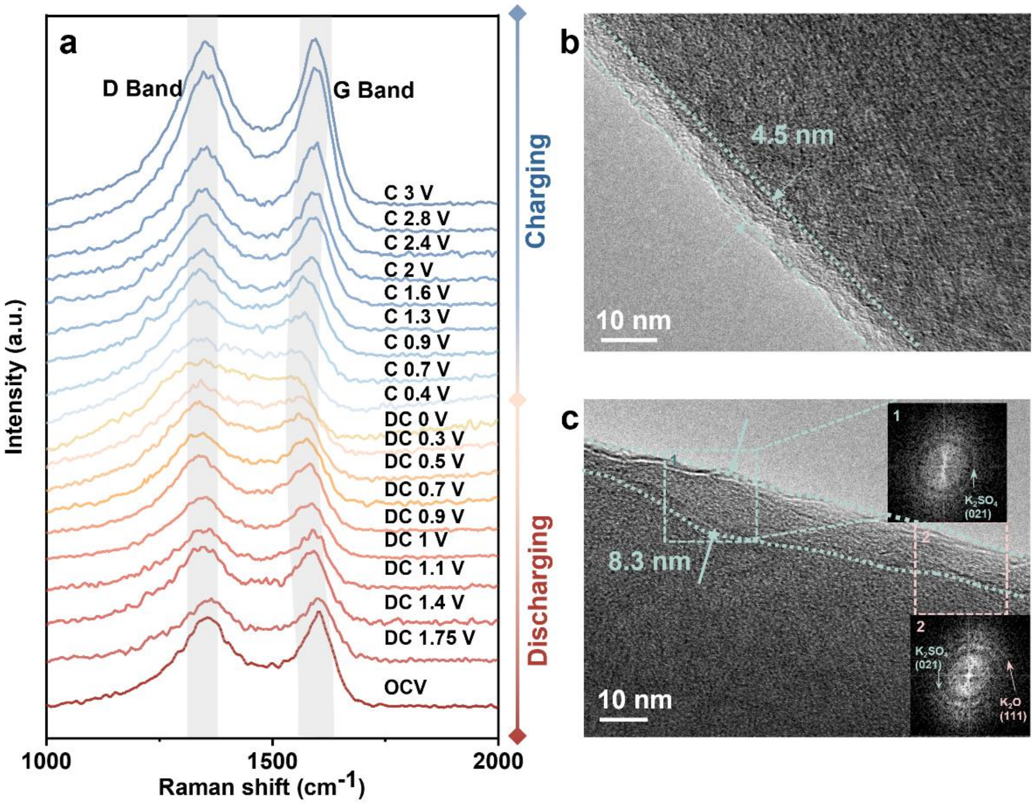

Fig. 4. (a) In-situ Raman plots of CNF electrode using the electrolyte of 1M KFSI in THF; TEM images of third-cycled CNFs in (b) 1M KFSI in THF and (c) 1M KFSI in EC/DMC with corresponding FFT patterns in the marked selected area at 50 mA g^{-1}.

The dramatic difference in the SEI morphology and the resulting electrochemical performance inspires us to get further insight into their chemical compositions. XPS spectra of C 1s, K 2p, O 1s, and F 1s are collected. A significant amount of organic species are observed, signified by the C−O (285.9 eV), C=O (286.6 eV) in C 1s spectra, C−O (532.14 eV), and C=O (531.1 eV) in O 1s (Fig. 5a-b). Parallelly, the K−O (292.8, 295.4 eV), K−F (293.7, 296.3 eV), CO_3^{2-} (288.2 eV) in K 2p spectra, with the K−F (683.6, 685.3 eV) and S−F (686.9, 688.2 eV) in F 1s spectra (Fig. 5c) reflect the inorganic components. In general, both the SEIs formed in ether and ester-based electrolytes have a composite structure with the inorganic species distributed in the organic matrix. The SEIs in THF electrolyte has a higher overall content of the inorganic components, as suggested by the lower carbon content of 72.8at.% compared to 77.7 at.% for the one in EC/DMC counterpart (Fig. 5d). The reason lies in the strong solvation of EC/DMC as discussed before, leading to the more severe decomposition of the solvent that mainly contributes to the organic species. Additionally, the stronger peak of CO_3^{2-} implies more solvent decomposition in the EC/DMC system. In comparison, more FSI^- are coordinated with the K^+ in THF electrolytes [30, 42], resulting in the significant anion decomposition to form the inorganic components, which can be reflected by the higher F content (Fig. 5c).

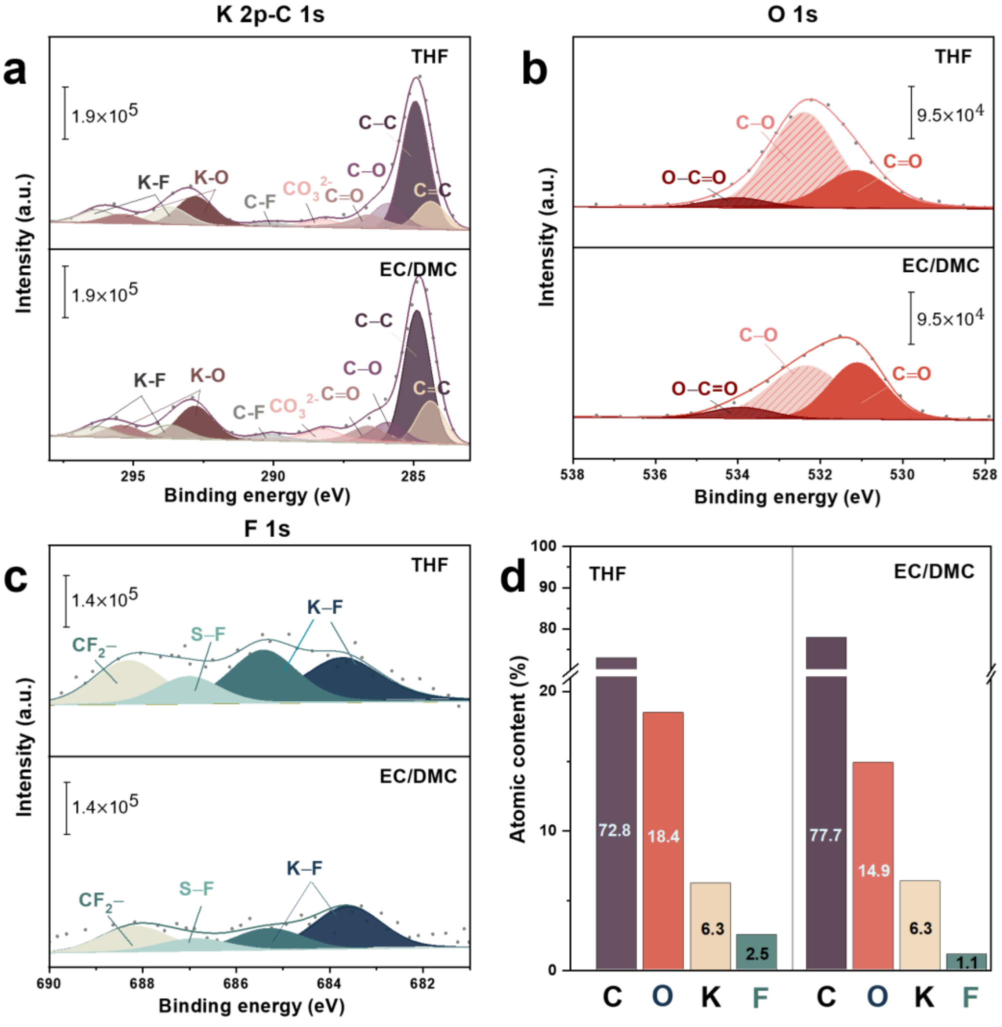

Fig. 5. The surficial composition analyzed by XPS. (a) K 2p-C 1s, (b) O 1s, and (c) F

1s spectra of CNFs after 3 cycles at 50 mA g^{-1} using electrolyte of 1M KFSI in THF or 1M KFSI in EC/DMC; (d) The atomic fractions of pristine CNFs cycled in 1M KFSI in THF or 1M KFSI in EC/DMC.

The K−F and S−F peaks for the THF system are more distinct than those in EC/DMC system, implying a higher proportion of K−F and S−F coordination and more inorganic components (like KF) from the FSI^- decomposition in the SEI under THF electrolyte. Moreover, the SEI in the THF system possesses 2.5at.% F, which is twice larger than that of the EC/DMC counterpart (1.1at.%) (Fig. 5d). Under the pre-condition that both solvents (THF and EC/DMC) contain no F element, the fluorine-rich SEIs in THF electrolyte are mainly from the decomposition of anion FSI. The rich F species could potentially benefit from the charge transfer, as widely observed in the LiF counterpart [43, 44]. Furthermore, in TEM figures, the inorganic components are almost amorphous for the SEI in the THF electrolyte, whereas crystallized particles are observed for the ones in EC/DMC electrolytes. Compared to the crystalline phase, the amorphous one is preferable for boosting ionic conductivity [45, 46]. In short, the thin and homogeneous SEIs in THF electrolytes significantly contribute to the superior rate performance.

4. Conclusion

We prepare a CNF film by electrospinning lignin and PAN, which serves as a freestanding electrode to probe the effect of interfacial chemistry on the kinetics of hard carbon anodes. We examine the physical and chemical properties of different solvents to screen the potential electrolytes for regulating the K ion solvation structure. The THF with low polarity and donor number is selected because of the weak K-solvent interaction, as confirmed by the Raman analysis. Such low solvation brings about several advantages. Firstly, it inhibits the solvent co-intercalation that occurs in the most widely investigated DME electrolyte, which deteriorates the electrode stability. Secondly, the facile de-solvation process would enhance the K ion insertion. Most importantly, a considerable amount of FSI^- enters the solvation sheath, leading to an inorganic-rich SEI that benefits the charge transfer. HRTEM images indicate the SEI formed in the THF electrolyte is more uniform and thinner than the one in the EC/DMC counterpart, further boosting the stability and kinetics across the SEI. Consequently, the CNFs show superior rate capability (143 mAh g^{-1} at 1.5 A g^{-1}) and cyclic performance in the THF-based electrolyte even at 0 °C. These results suggest that the hard carbon anodes could sustain the high rate PIBs with the rational electrolyte design, where cyclic ether may offer unique merits.

CRediT authorship contribution statement

Z. Y.: conceptualization, methodology, formal analysis, investigation, writing—original draft & editing. Q. L.: methodology. C. C.: TEM investigation. Y. Z.: TEM investigation, writing—review & editing. B.Z.: conceptualization, methodology, resources, supervision, writing–review & editing, project administration, funding acquisition.

Declaration of competing interest

The authors declare no conflict of interest.

Acknowledgments

This work was supported by the Environment and Conservation Fund (84/2020) of

Hong Kong.

References

[1] X. Min, J. Xiao, M. Fang, W. Wang, Y. Zhao, Y. Liu, A.M. Abdelkader, K. Xi, R.V. Kumar, Z. Huang, Energy & Environmental Science, 14 (2021) 2186-2243.

[2] J.L. Xia, D. Yan, L.P. Guo, X.L. Dong, W.C. Li, A.H. Lu, Advanced Materials, 32 (2020) e2000447.

[3] J. Liao, Y. Han, Z. Zhang, J. Xu, J. Li, X. Zhou, Energy & Environmental Materials, 4 (2021) 178-200.

[4] Y. Zhang, Y. Du, B. Song, Z. Wang, X. Wang, F. Wan, X. Ma, Journal of Power Sources, 545 (2022) 231920.

[5] N. Li, Y. Yao, T. Lv, Z. Chen, Y. Yang, S. Cao, T. Chen, Journal of Power Sources, 488 (2021) 229460.

[6] K. Kubota, M. Dahbi, T. Hosaka, S. Kumakura, S. Komaba, Chem Rec, 18 (2018) 459-479.

[7] Z. Jian, W. Luo, X. Ji, Journal of the American Chemical Society, 137 (2015) 11566-11569.

[8] J. Li, Y. Hu, H. Xie, J. Peng, L. Fan, J. Zhou, B. Lu, Angewandte Chemie International Edition, 61 (2022) e202208291.

[9] E. Peled, Journal of The Electrochemical Society, 126 (1979) 2047-2051.

[10] E. Peled, D. Golodnitsky, G. Ardel, Journal of The Electrochemical Society, 144 (1997) L208-L210.

[11] S. Jiao, X. Ren, R. Cao, M.H. Engelhard, Y. Liu, D. Hu, D. Mei, J. Zheng, W. Zhao,

Q. Li, N. Liu, B.D. Adams, C. Ma, J. Liu, J.-G. Zhang, W. Xu, Nature Energy, 3 (2018) 739-746.

[12] J. Zhang, Z. Cao, L. Zhou, G.-T. Park, L. Cavallo, L. Wang, H.N. Alshareef, Y.-K. Sun, J. Ming, ACS Energy Letters, 5 (2020) 3124-3131.

[13] J. Yang, Y. Zhai, X. Zhang, E. Zhang, H. Wang, X. Liu, F. Xu, S. Kaskel, Advanced Energy Materials, 11 (2021) 2100856.

[14] H. Tan, X. Du, R. Zhou, Z. Hou, B. Zhang, Carbon, 176 (2021) 383-389.

[15] Z. Jian, Z. Xing, C. Bommier, Z. Li, X. Ji, Advanced Energy Materials, 6 (2016) 1501874.

[16] S. Alvin, H.S. Cahyadi, J. Hwang, W. Chang, S.K. Kwak, J. Kim, Advanced Energy Materials, 10 (2020) 2000283.

[17] B. Zhang, F. Kang, J.-M. Tarascon, J.-K. Kim, Progress in Materials Science, 76 (2016) 319-380.

[18] J.L. Yang, Z.C. Ju, Y. Jiang, Z. Xing, B.J. Xi, J.K. Feng, S.L. Xiong, Advanced Materials, 30 (2018) 1700104.

[19] T. Zhang, Z. Mao, X. Shi, J. Jin, B. He, R. Wang, Y. Gong, H. Wang, Energy & Environmental Science, 15 (2022) 158-168.

[20] J. Zhao, X. Zou, Y. Zhu, Y. Xu, C. Wang, Advanced Functional Materials, 26 (2016) 8103-8110.

[21] L. Wang, J. Yang, J. Li, T. Chen, S. Chen, Z. Wu, J. Qiu, B. Wang, P. Gao, X. Niu, H. Li, Journal of Power Sources, 409 (2019) 24-30.

[22] T. Hosaka, K. Kubota, H. Kojima, S. Komaba, Chemical Communications, 54

(2018) 8387-8390.

[23] Y. Lei, J. Wang, D. Han, F. Yuan, H. Wang, R. Zhao, D. Huang, Y. Wu, B. Zhang, D. Zhai, F. Kang, Carbon, 196 (2022) 229-235.

[24] L. Qin, N. Xiao, J. Zheng, Y. Lei, D. Zhai, Y. Wu, Advanced Energy Materials, 9 (2019) 1902618.

[25] P.N. Le Pham, V. Gabaudan, A. Boulaoued, G. Åvall, F. Salles, P. Johansson, L. Monconduit, L. Stievano, Energy Storage Materials, 45 (2022) 291-300.

[26] L. Li, L. Liu, Z. Hu, Y. Lu, Q. Liu, S. Jin, Q. Zhang, S. Zhao, S.-L. Chou, Angewandte Chemie International Edition, 59 (2020) 12917-12924.

[27] Z. Tang, H. Wang, P.F. Wu, S.Y. Zhou, Y.C. Huang, R. Zhang, D. Sun, Y.G. Tang, H.Y. Wang, Angewandte Chemie International Edition, 61 (2022) e202200475.

[28] H.J. Liang, Z.Y. Gu, X.X. Zhao, J.Z. Guo, J.L. Yang, W.H. Li, B. Li, Z.M. Liu, W.L. Li, X.L. Wu, Angewandte Chemie International Edition, 60 (2021) 26837-26846.

[29] D. Wang, X. Du, B. Zhang, Small Structures, 3 (2022) 2200078.

[30] Y.X. Yao, X. Chen, C. Yan, X.Q. Zhang, W.L. Cai, J.Q. Huang, Q. Zhang, Angewandte Chemie International Edition, 60 (2021) 4090-4097.

[31] Q. Li, Z. Cao, W. Wahyudi, G. Liu, G.-T. Park, L. Cavallo, T.D. Anthopoulos, L. Wang, Y.-K. Sun, H.N. Alshareef, J. Ming, ACS Energy Letters, 6 (2021) 69-78.

[32] J. Holoubek, H. Liu, Z. Wu, Y. Yin, X. Xing, G. Cai, S. Yu, H. Zhou, T.A. Pascal, Z. Chen, P. Liu, Nature Energy, 6 (2021) 303-313.

[33] C. Wang, A.J. Appleby, F.E. Little, Journal of Electroanalytical Chemistry, 519 (2002) 9-17.

[34] L. Fan, R. Ma, Q. Zhang, X. Jia, B. Lu, Angewandte Chemie International Edition, 58 (2019) 10500-10505.

[35] X. Chen, J. Tian, P. Li, Y. Fang, Y. Fang, X. Liang, J. Feng, J. Dong, X. Ai, H. Yang, Y. Cao, Advanced Energy Materials, 12 (2022) 2200886.

[36] S. Komaba, W. Murata, T. Ishikawa, N. Yabuuchi, T. Ozeki, T. Nakayama, A. Ogata, K. Gotoh, K. Fujiwara, Advanced Functional Materials, 21 (2011) 3859-3867.

[37] L.J. Hardwick, P.W. Ruch, M. Hahn, W. Scheifele, R. Kotz, P. Novak, Journal of Physics and Chemistry of Solids, 69 (2008) 1232-1237.

[38] H. Tan, R. Zhou, B. Zhang, Journal of Power Sources, 506 (2021) 230179.

[39] W. Huang, P.M. Attia, H. Wang, S.E. Renfrew, N. Jin, S. Das, Z. Zhang, D.T. Boyle, Y. Li, M.Z. Bazant, B.D. McCloskey, W.C. Chueh, Y. Cui, Nano Letters, 19 (2019) 5140-5148.

[40] Y. Gao, Z. Hou, R. Zhou, D. Wang, X. Guo, Y. Zhu, B. Zhang, Advanced Functional Materials, 32 (2022) 2112399.

[41] C. Cao, I.I. Abate, E. Sivonxay, B. Shyam, C. Jia, B. Moritz, T.P. Devereaux, K.A. Persson, H.-G. Steinrück, M.F. Toney, Joule, 3 (2019) 762-781.

[42] T.D. Pham, K.-K. Lee, Small, 17 (2021) 2100133.

[43] E. Peled, S. Menkin, Journal of The Electrochemical Society, 164 (2017) A1703-A1719.

[44] M. He, R. Guo, G.M. Hobold, H. Gao, B.M. Gallant, Proceedings of the National Academy of Sciences, 117 (2020) 73-79.

[45] J. Huang, X. Guo, X. Du, X. Lin, J.-Q. Huang, H. Tan, Y. Zhu, B. Zhang, Energy

& Environmental Science, 12 (2019) 1550-1557.

[46] F. Tian, M.D. Radin, D.J. Siegel, Chemistry of Materials, 26 (2014) 2952-2959.